Check for updates

Superior visible light photocatalytic performance of reticular BiVO$_4$ synthesized *via* a modified sol–gel method

Lingyun Zhang, [iD] *[ab] Zhenxiang Dai,[a] Ganhong Zheng,*[a] Zifeng Yao[a] and Jingjing Mu[a]

Reticular BiVO$_4$ catalysts were successfully synthesized *via* a modified sol–gel method. Here, citric acid (CA) was used as the chelating agent and ethylenediaminetetraacetic acid (EDTA) was used as the chelating agent and template. Furthermore, the effects of pH values and EDTA on the structure and morphology of the samples were studied. We determined that EDTA and pH played important roles in the determination of the morphology of the as-prepared BiVO$_4$ samples. Photocatalytic evaluation revealed that the reticular BiVO$_4$ exhibited superior photocatalytic performance characteristics for the degradation of methylene blue (MB) under visible-light ($\lambda > 400$ nm) exposure, about 98% of the MB was found to degrade within 50 min. Moreover, the degradation kinetics of MB was in good agreement with pseudo-first-order kinetics. The obtained apparent reaction rate constant k_{app} of reticular BiVO$_4$ was much higher than that of BiVO$_4$ synthesized by the citric acid sol–gel method.

1. Introduction

During the last decade, semiconductor photocatalysts have captured substantial attention due to a variety of potential energy and environmental applications. By means of the combination of a semiconductor and appropriate electromagnetic radiation, it is possible to induce a charge separation in the semiconductor that produces free electrons (e$^-$) and holes (h$^+$) in its conduction band (CB) and valence band (VB), respectively. If the formed electron–hole pair is not recombined, both species can migrate separately to the semiconductor surface and then participate in oxidation (h$^+$) or reduction (e$^-$) reactions with chemical compounds adsorbed on the surface of the semiconductor. Since the process does not alter the composition of the semiconductor, the material may be used in industrial applications as a photocatalyst.[1–5] Titanium dioxide catalysts have been the most promising candidates, owing to their superior redox ability, chemical inertness, non-toxicity, and comparatively low cost, as well as their excellent photo-/chemical corrosion-resistant stability. Titanium dioxide catalysts have also been commercially applied as a self-cleaning coating on buildings and glass materials in some countries. Nevertheless, considering its large band gap ($\sim$3.0 eV for rutile and 3.2 eV for anatase), titanium dioxide catalysts can only

absorb around 4% the whole solar light in the ultraviolet light, resulting in low efficiency of the solar energy. Therefore, the development of novel photocatalysts with visible light range (around 45% of the solar spectrum), high efficiency and good stability remains a critical, albeit unmet, scientific goal for practical applications.[6–8]

Recently, various research fields have focused on the morphological design and development of non-TiO$_2$-based single-phase oxide photocatalysts with visible light range, including YVO$_4$, Bi$_2$MoO$_6$, and Bi$_2$WO$_6$ and so on.[9–11] Among the different oxides designing an efficient sunlight-driven photocatalyst system, bismuth vanadate (BiVO$_4$), which represents an effective photocatalyst for energy production and pollutant degradation under visible-light range, has been explored as a key solution.[12,13] The activity of this photocatalyst is closely related to the structure, crystallite dimension, size, morphology and surface appearance, which in return are generally thought to depend on the synthetic methods and the preparation conditions used.[14] However, some challenges, such as enhancing the specific surface area, lowering the migration distance for the photo-generated electron and hole pairs, and preventing the recombination of electron and hole pairs, remain when trying to improve the photocatalytic performance of BiVO$_4$. For this reason, various methods have been utilized to prepare BiVO$_4$ with the different morphology, including a conventional solid-state reaction, sol–gel method, coprecipitation, pulsed laser deposition, and hydrothermal processes.[15–19] Particularly, the sol–gel method won increasingly more importance in materials science as it requires only simple

[a]*Anhui Key Laboratory of Information Materials and Devices, School of Physics and Materials Science, Anhui University, Hefei 230039, China. E-mail: ghzheng@ahu.edu.cn; lingyunf@126.com*

[b]*Department of Chemical and Material Engineering, Hefei University, Hefei 230601, China*

equipment and low process temperature, compared to the traditional methods of powders.[20,21]

Herein, reticular $BiVO_4$ catalysts were successfully synthesized by a modified sol–gel combustion method. Citric acid (CA) and ethylenediaminetetraacetic acid (EDTA) were used as chelating and shape-controlling agents. Both EDTA and pH value have been shown to play vital roles in the formation of the catalysts. Methylene blue (MB) was employed to evaluate the photocatalytic activities of as-prepared $BiVO_4$ samples under visible-light ($\lambda > 400$ nm) irradiation. The results indicated that 98% of the MB was degraded under visible-light irradiation within 50 min, demonstrating that the as-prepared reticular $BiVO_4$ exhibit excellent photocatalytic performance characteristics.

2. Experimental

2.1. Synthesis of materials

All chemicals used in this work were of analytical grade and used as received without further purification. In a typical preparation process, 0.01 mol of $Bi(NO_3)_3 \cdot 5H_2O$ and 0.02 mol of citric acid (CA) were dissolved in 40 mL of 2.0 mol L^{-1} HNO_3 and stirred for about 30 min until a clear solution A was obtained. 0.01 mol of NH_4VO_3 and 0.02 mol of CA were dissolved in 40 mL of aqueous ammonia and stirred until a light yellow solution B was obtained. After addition of solution A to solution B, a uniform transparent dark green solution C was obtained. Meanwhile, 5 mmol of EDTA dissolved in aqueous ammonia was added to C. The 0.002 mol −0.01 mol of EDTA was added to obtain a light blue solution D. The pH of the mixture was adjusted with ammonia solution. The obtained sol was stirred for 30 min and then heated to 75 °C for water evaporation. The formed gel was annealed in air at different temperatures for 3.0 h with a heating rate of 2 °C min^{-1}. As a consequence, fluffy $BiVO_4$ powders were successfully obtained after the calcination process. The as-obtained product was denoted as S1–S10, respectively, as described in Table 1. For comparison purposes, we also adopted by the citric acid sol–gel method (without EDTA) to prepare the $BiVO_4$ photocatalyst (denoted as S11).

2.2. Photocatalytic activity

The $BiVO_4$ samples were evaluated via degradation of MB solution under visible light. Typically, 0.15 g of a photocatalyst were added to 100 mL of a MB solution (4.2×10^{-5} mol L^{-1}) and stirred in the dark for 50 min to achieve an adsorption–desorption equilibrium. The suspension was then irradiated using a 300 W Xenon lamp. The experimental temperature was kept at 25 on2 °C by circulating water through an external cooling jacket. At an irradiation interval of every 10 min, 4 mL suspensions were removed and filtered to remove the photocatalyst particles with water syringe filter membrane of $\phi 13$ mm $\times$ 0.22 mm. The concentrations of methylene blue were monitored with a Unicosh V-1600 UV-vis spectrophotometer using an absorbance wavelength of 664 nm during the photodegradation process. The photodegradation efficiency of the MB was estimated according to the following formula: $\eta = C/C_0$, where C_0 and C are the absorbances of the pre- and post-irradiation of the MB solution.

2.3. Characterization

Thermogravimetry was implemented on a thermal gravimetric analyzer (TG, Q500, TA) under N_2 atmosphere. XRD data was collected on a X-ray diffraction instrument (XRD, TD3500, Tongda) using Cu-Kα radiation ($\lambda = 0.15406$ nm) to characterize the crystal structures of the as-prepared sample. The morphology and size of the particles were studied using a field-emission scanning electron microscope (SEM, SU8010, Hitachi) and a (high resolution) transmission electron microscope (TEM, JEOL JEM-2100) and an energy dispersive spectrometer (EDS, Hitachi SU8010). The Brunauer–Emmett–Teller (BET) surface area of the samples was determined by a N_2 adsorption–desorption method using an Autosorb-iQ automatic specific surface and a porosity analyzer at 77.3 K. The UV-vis absorption spectra were obtained with a Jasco V-650 spectrophotometer. Photoluminescence (PL) spectra were analyzed using a Jasco FP-8500 fluorescence spectrometer with a 450 W Xenon lamp as light source. FT-IR spectra of phosphorus were recorded on a Nicolet IS-50 spectrometer with KBr pellet technique from 4000 to 400 cm^{-1}. All measurements were performed at room temperature.

3. Results and discussion

3.1. Crystal phase composition

The thermal properties of the used precursor are shown in Fig. 1. Three processes of weight loss are shown to have occurred as can be seen by inspection of the TG curve from room temperature to 700 °C. The first process of weight took place between room temperature and 175 °C and a weight loss of 1.7% could be attributed to the removal of adsorbed water on the surface of or the residual water molecules. The second weight loss in the range of 175 to 330 °C was related to the combustion of CA and EDTA and the corresponding weight loss corresponded to about 6.3%. The third step from 330 to 435 °C was related to the decomposition of the residual nitrates.[22] The total weight loss accounts for about 9.9%. No further obvious

Table 1 The different molar ratios of EDTA : CA : Bi and pH value obtained samples

Sample	S1	S2	S3	S4	S5	S6	S7	S8	S9	S10
EDTA : CA : Bi (mol)	0.5 : 4 : 1	(0.5 + 0.2) : 4 : 1	(0.5 + 0.4) : 4 : 1	(0.5 + 0.5) : 4 : 1	(0.5 + 0.6) : 4 : 1	(0.5 + 1.0) : 4 : 1	—	—	—	—
pH value	—	—	—	—	—	—	4.0	5.0	9.0	10.0

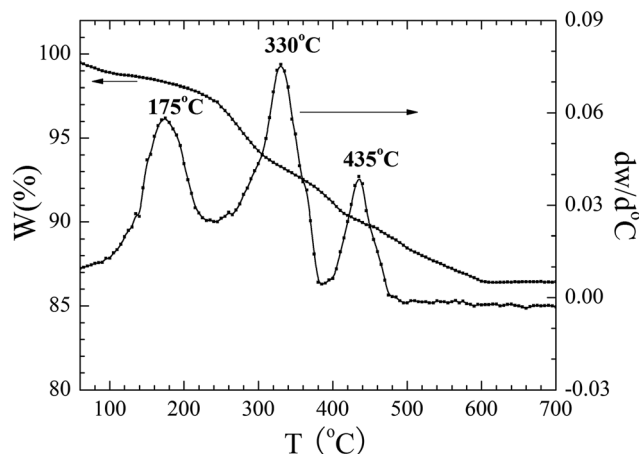**Fig. 1** TG curves of dried precursor-gel the BiVO₄ samples in N₂.

weight loss could be detected above 600 °C, indicating that all precursor compounds decomposed completely. The above three processes of weight loss from room temperature to 700 °C are also shown in Fig. 1.

According to the thermal analysis results, the precursors were treated at various temperatures from 160 to 550 °C in order to crystallize. The XRD patterns of the corresponding samples are shown in Fig. 2(a). After heat treatment at 350 °C, several weak diffraction peaks could be observed, highlighting the initial crystallization event of the precursors. When the temperature was increased to 400 °C, the crystallization behavior of the samples increased and prominent peaks could be indexed to monoclinic BiVO₄ except for several minor peaks at $2\theta = 25.7°$, 27.7° and 32.3°, which correspond to Bi₂O₃ as an impurity. As the temperature increased to 450 °C, the peaks corresponding to Bi₂O₃ disappeared. The diffraction peaks at 18.9, 28.9, 30.5, 35.2, 46.7, 47.3 and 53.3 could be ascribed to be the monoclinic BiVO₄ structure (JCPDS, no. 83-1699). Upon increasing the calcination temperature to 500 °C and 550 °C, respectively, the obtained samples were all in a monoclinic scheelite phase. No impurity peaks could be observed, indicating that all samples were of phase-pure monoclinic BiVO₄. The crystal sizes of the samples were calculated according to the Debye–Scherrer's formula: $D = \dfrac{K\lambda}{(B^2 - b^2)^{0.5}\cos\theta}$, where D is the

crystal size; λ represents the wavelength of X-ray radiation ($\lambda = 0.15406$ nm), K is a constant at 0.89, B and b are the peak widths of the half-maximum height of the (112) diffraction peak and of the equipment broadening, respectively.[23] The crystal sizes of BiVO₄ powders calcined at 400, 450, 500 and 550 °C were determined to be 27.2, 28.9, 29.1 and 29.9 nm, respectively. The latter finding indicates that the crystal sizes increased with increasing calcination temperatures.

Fig. 2(b) and (c) show the XRD patterns of the BiVO₄ samples at different EDTA to CA ratios and pH values. It is worth noting that in the sol–gel process of preparing samples, the calcination temperature of precursors was kept at 450 °C for 3.0 h. We found that all these XRD patterns can be well indexed as the pure scheelite tetragonal structure (I2/b space group) and are in good agreement with the values of the standard card (JCPDS, no. 83-1699). No other impurity phase could be detected in these samples. The crystal sizes of the BiVO₄ samples were calculated according to Debye–Scherrer's formula as shown in Table 2.

To investigate the chemical composition and chemical bonding of the composites, FT-IR was carried out and the corresponding spectra are shown in Fig. 3. The two bands at about 3389 and 1680 cm⁻¹ may be attributed to the stretching and deformation vibration of the O–H groups of chemisorbed and/or physisorbed water molecules. The spectra also show the bending vibration of NO₃⁻ anions at 1380 cm⁻¹. This result suggests that NO₃⁻ anions are present in the BiVO₄ precursors at 160 °C. The symmetric stretching vibration band at 482 cm⁻¹ can be assigned to the stretching vibration bands of VO₄⁻³ at 160 and 350 °C. The characteristic bands of BiVO₄, which include the V–O symmetric and stretching vibrations at 827 cm⁻¹ and 738 cm⁻¹ as well as the bending vibration band of Bi–O at 678 cm⁻¹, can also be observed in all samples.[24,25] From the FT-IR spectra, the organics in the gel fibers were completely removed by heat treatment at 450 rC for 3.0 h, with a heating rate of 2 °C min⁻¹. Therefore, the FT-IR, XRD and TG characterization results show that the optimal calcination temperature of the BiVO₄ sample is 450 °C.

3.2. Morphologies and microstructures

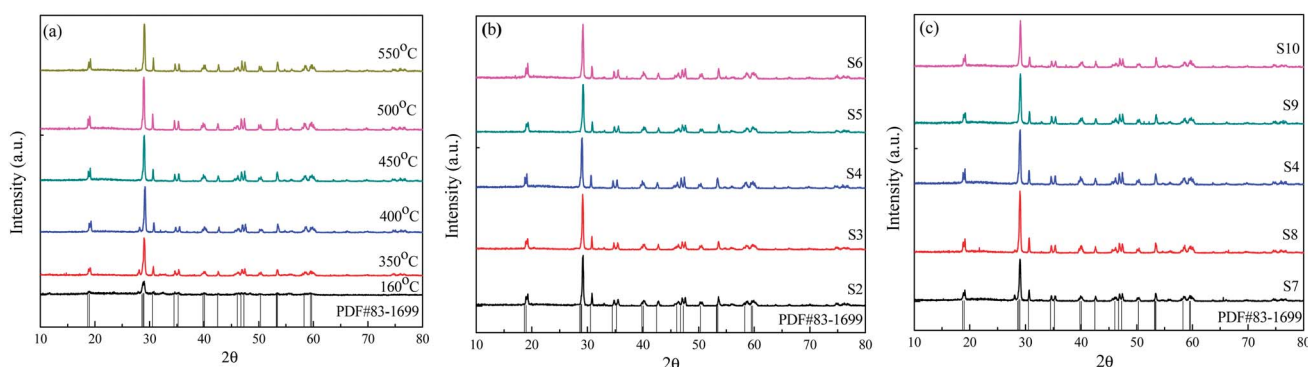Fig. 4–6 show the SEM, TEM and high-resolution TEM images as well as the EDS patterns of the reticular BiVO₄ samples.

Fig. 2 The XRD patterns of the reticular BiVO₄ samples: (a) different calcination temperatures, (b) different EDTA to CA, (c) different pH values.

Table 2 Physical properties of the reticular $BiVO_4$ samples

Sample		S_{BET} (m^2 g^{-1})	Pore volume (cm^3 g^{-1})	Pore size (nm)	B (°)	Crystallite size (nm)
Calcination temperature	400 °C	5.202	0.005	30.5	0.298	27.2
	450 °C	5.228	0.009	30.5	0.281	28.9
	550 °C	3.040	0.006	30.5	0.271	29.9
EDTA to CA	S2	4.867	0.008	35.2	0.289	28.1
	S4	5.228	0.009	30.5	0.281	28.9
	S6	3.26	0.011	48.9	0.285	28.5
pH value	S7	4.098	0.006	48.9	0.268	30.3
	S4	5.228	0.009	30.5	0.281	28.9
	S10	2.782	0.003	49.1	0.262	30.9

Fig. 4(a) shows that the as-prepared samples without any dissociated EDTA exhibit a significant agglomeration due to calcining treatment at higher temperature. Fig. 4(b–j) show the $BiVO_4$ samples displaying reticular sheet-like structures. However, the employment of the EDTA template and the pH value changes are vastly different in terms of their structural quality. As is well known, EDTA and the pH value play significant key roles in the control of the morphologies and microstructures of the particles. An increase in the amount of EDTA or pH value is not beneficial to the formation of the reticulated architecture for the $BiVO_4$ samples. Notably, a significant increase in EDTA or pH even leads to substantial destruction of the reticular sheet-like structure. The structure of the reticular $BiVO_4$ samples were further studied by energy dispersive X-ray spectroscopy (EDS) and the corresponding results are shown in Fig. 5. Presumably, Bi, V, and O elements distribute well within the selected area. The EDS elemental spectra results also confirm the multi-component structure of the selected sample.

Fig. 6 shows typical TEM and HRTEM results for $BiVO_4$ samples. The TEM images in Fig. 6(a) indicate that the reticular $BiVO_4$ samples are hierarchically assembled from hundreds of nanorods with lengths in the range of 250 to 800 nm and

diameters of about 50 to 150 nm. The selected-area electron diffraction (SAED) pattern in Fig. 6(b) shows that $BiVO_4$ nanorods are of high crystallinity, with a tetragonal crystal-phase consistent with the XRD results highlighted in Fig. 1. The further microstructures of the $BiVO_4$ nanorods were examined by HRTEM studies as shown in Fig. 6(c). The presence of clear lattice fringes with perfect single crystal structure could be determined. The spacing of all samples between two adjacent horizontal and vertical lattice planes was 0.475 nm and 0.312 nm, close to the values for d_{101} (0.47487 nm) and d_{103} (0.31198 nm), respectively.

Taken in concert, EDTA is found to play a critical role in the control of the morphologies and microstructures of the $BiVO_4$ products. It is clear in this context that a strong ligand, EDTA, is not only required to form a stable complex with Bi^{3+}, but also acts as a soft template that directly affects the facet growth of the nanocrystals. As a strong chelator, EDTA reacts with Bi^{3+} to form stable Bi–EDTA complexes. The addition of EDTA to the reaction system may provide a soft growth process, whereas the crystal growth is more likely to comply with the intrinsic crystal growth behavior. In other words, EDTA has the ability to balance the growth rate of different facets, ultimately leading to a restriction of crystal growth. When the molar ratio of EDTA to CA increases up to $(0.5 + 0.2) : 4$, only layer structures were formed (Fig. 4(b)). Meanwhile, without the addition of EDTA and while keeping other conditions constant, mainly agglomeration particles could observed as shown in Fig. 4(a). Through increasing the molar ratio of EDTA to CA, the reticular structure of the $BiVO_4$ nanocrystals gradually formed and later destructed as indicated in Fig. 4(c–f), reaching a optimum condition at the molar ratio of EDTA to CA equal to $(0.5 + 0.5) : 4$ due to the appropriate chelation and capping abilities. From inspection of Fig. 6(a–c) it can be determined that the $BiVO_4$ nanorods grow along the c-axis direction. Therefore, it can be concluded that the Bi^{3+} ions form stable coordination complexes with EDTA in aqueous solution and because of this feature, the surface adsorption of EDTA on the (100) planes exhibits a higher coverage than that on the (001) and (010) planes, ultimately resulting in crystal growth direction along [100]. When the EDTA/CA ratio was higher than $(0.5 + 0.2) : 4$, a preferential binding to the faces vertical to the c-crystal axis could be observed, resulting in a high growth aspect ratio of the reticular sheet-like $BiVO_4$ samples. While the EDTA/CA ratio reaches $(0.5$
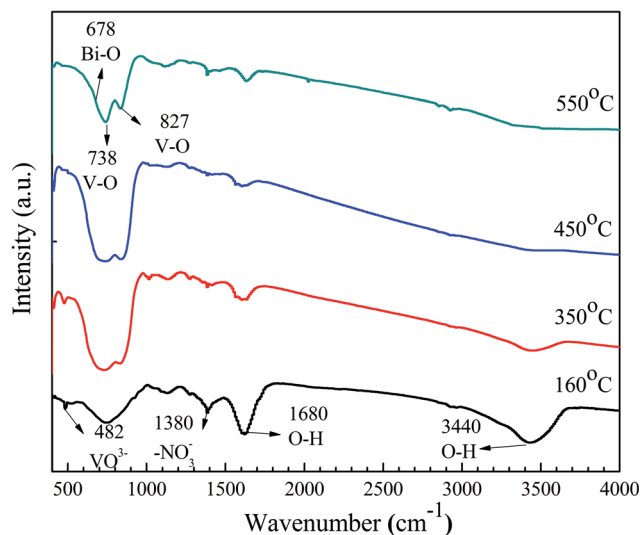

Fig. 3 FT-IR spectra of the $BiVO_4$ samples calcined at different temperature.

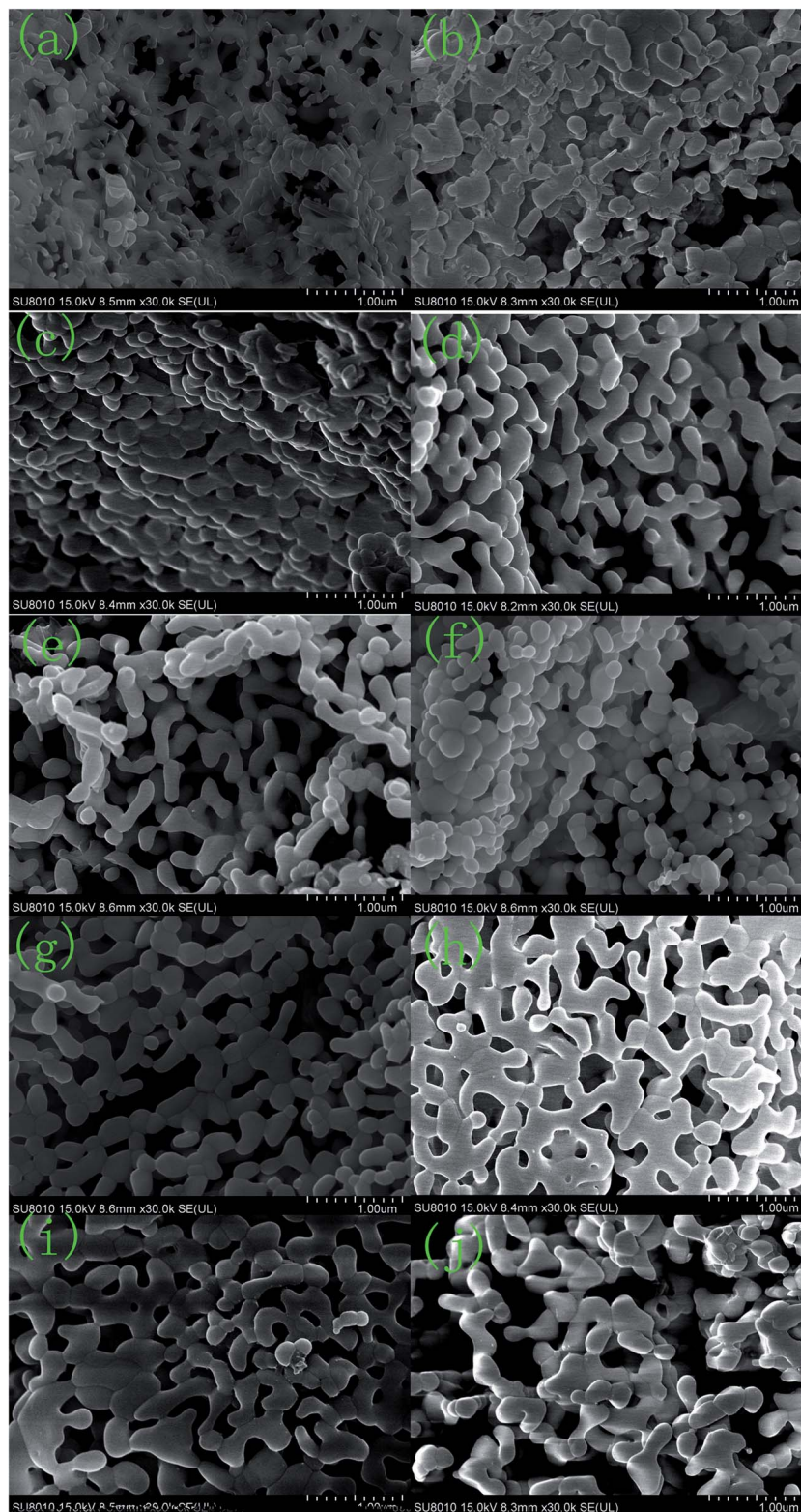**Fig. 4** SEM spectra of the reticular $BiVO_4$ samples: (a) S1, (b) S2, (c) S3, (d) S4, (e) S5, (f) S6, (g) S7, (h) S8, (i) S9, (j) S10.

+ 0.8) : 4, those faces vertical to the c-crystal axis were fully covered and other faces parallel to the c-crystal axis were also allowed to be adsorbed, resulting in a lower aspect ratio and a reticular sheet-like $BiVO_4$ shift to layer $BiVO_4$ as shown in Fig. 4(c–f). Based on the above analysis, both the surface adsorption of EDTA and the intrinsic crystal growth behavior play important role in determining the final crystal morphology.[26–29]
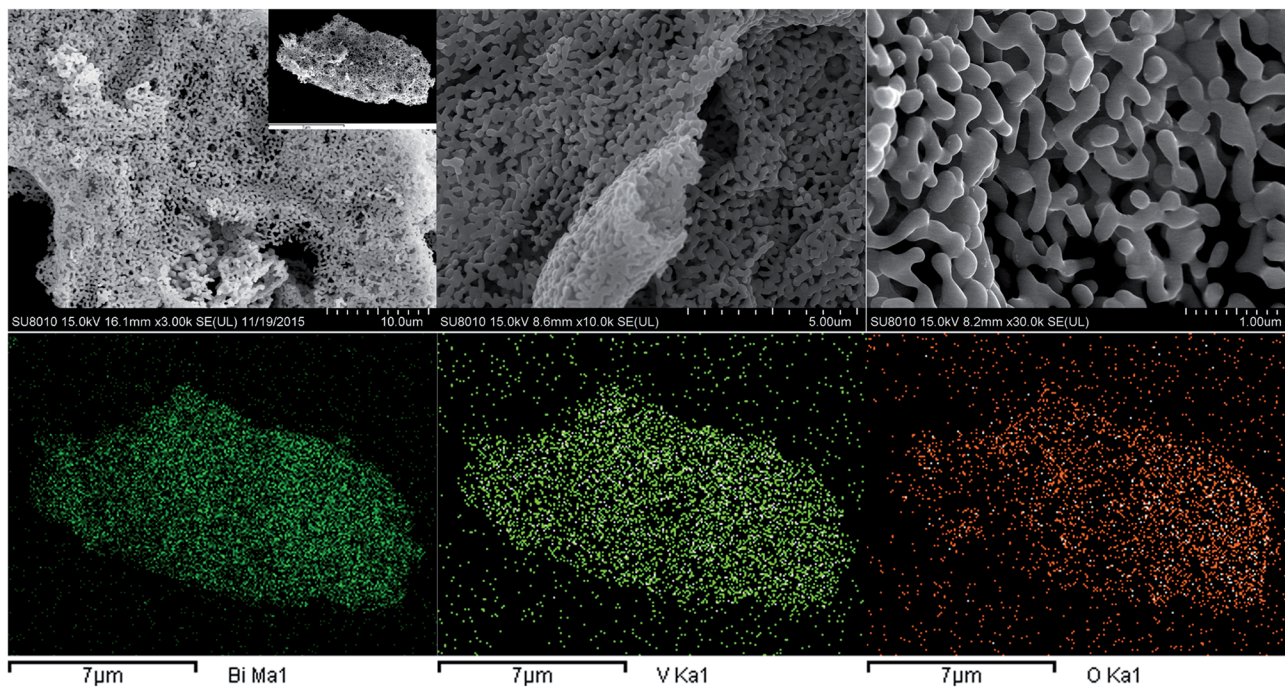
Fig. 5 SEM image and EDS spectra of S4 sample.

Concurrently, we found that the morphology of the $BiVO_4$ samples is also controlled by the pH value of the precursor solution. Although various studies have been carried out to explore the shape selectivity mechanism of the pH for this system, we believe that the tendency of minimizing the surface energy of the samples is crucial for the determination of the morphology of the samples. As the pH of the solution decreased to a value below 5.0, some EDTA precipitated from the solution due to a reduced solubility of EDTA. Upon increasing the solution pH beyond 9.0, amido groups began to chelate with Bi^{3+} and the ammonia concentration increased, resulting in an insufficient EDTA chelation with Bi^{3+}. At low pH or high pH, the c-crystal axis aspect ratio of the $BiVO_4$ samples were found to be reduced due to the weakened chelation ability of EDTA. Only when the pH value of the solution was in the range of 5.0–9.0, EDTA could adequately chelate with Bi^{3+}, resulting in a high growth aspect ratio of the reticular sheet-like $BiVO_4$ samples.

Therefore, a simple method was investigated to control the aspect ratio of the $BiVO_4$ nanocrystals by adjusting the pH value of the precursor solution.[30,31]

3.3. N_2 adsorption and desorption isotherm

Fig. 7 shows the N_2 adsorption and desorption isotherms of the reticular $BiVO_4$ sample as well as the corresponding pore size distribution curve. The isotherms exhibit a hysteresis loop with sharp adsorption and desorption branches at high relative pressure. The physisorption isotherms can be categorized as type IV, being representative of a mesoporous powder, which has been reported to be a clear advantage of degrading organic pollutants in water.[32] The pore size distribution can be calculated from the desorption branch of the isotherms by using a BJH model. The results shown in Table 2 indicate that the reticular $BiVO_4$ sample exhibits a most probable pore size of about 30–50 nm. The measured Brunauer–Emmett–Teller (BET)
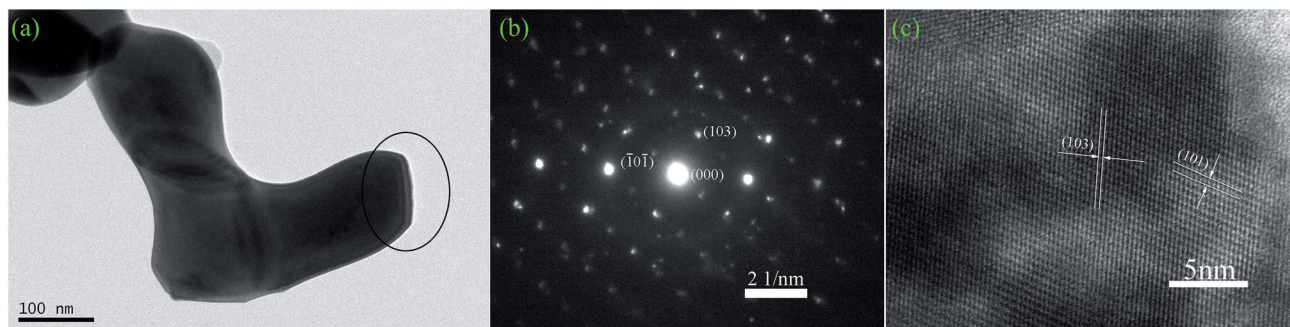

Fig. 6 Microstructure characteristic of S4 sample: (a) TEM image, (b) SAED pattern, (c) HRTEM image.
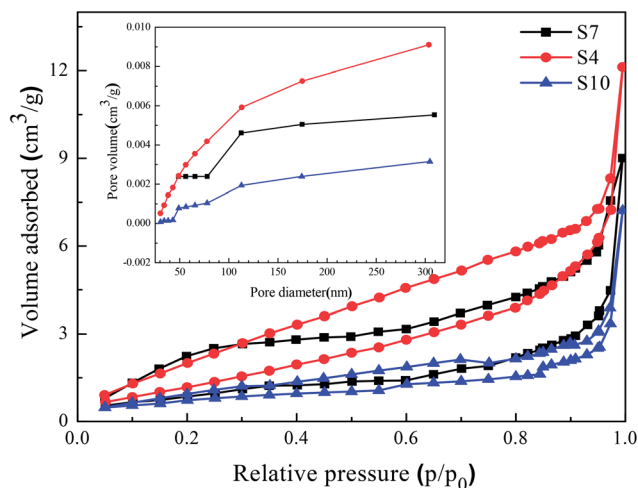
Fig. 7 N_2 adsorption–desorption isotherm curves of the reticular $BiVO_4$ samples synthesized with different pH values; the inset is the pore size distributions.

surface area of the reticular $BiVO_4$ sample is about 3.0–5.0 m^2 g^{-1}. However, the specific surface area of the samples is close and not large enough, indicating that the surface area is not the only reason for the varying photocatalytic activity. Zhou *et al.* have also confirmed that in this material the photo-activity is more closely related to the surface (or shape) of the structure than the actual surface area or other physical properties. It can be safely concluded that such a high photo-activity appears to be due to the presence of a distinctive morphology.[28,33]

3.4. Photoluminescence properties

UV-vis diffuse reflectance spectra of the obtained reticular $BiVO_4$ samples were recorded and are shown in Fig. 8. All samples exhibit absorption in the visible light range and the steep absorbance edges of all spectra indicate that the visible light absorption is not due to the transition from impurity levels

but the band gap transition.[34] The band gap energies (E_g) of the prepared samples can be calculated from the UV-vis absorption spectra data using the following formula: $\alpha h\nu = A(h\nu - E_g)^{n/2}$, where α, ν, A and E_g are the absorption coefficient, the light frequency, a constant and the band gap energy, respectively. The value for n is determined by the type of optical transition of a semiconductor ($n = 1$ for direct transition and $n = 4$ for indirect transition). Because the value for n of m-$BiVO_4$ is 1, the E_g of m-$BiVO_4$ could be estimated from the plot of $(\alpha h\nu)^2$ *versus* ($h\nu$). From inspection of Fig. 8, E_g for the different samples could be estimated to be between 2.41 and 2.45 eV (Table 3), higher than the values reported in the literature.[29] The obvious blue shift of the band gap absorption edge is likely due to the following notions: the diameter of the particles was reduced to nano-size and the electrons bound in its field, with the states of electronic density being discrete. This ultimately limits the freedom of movement of electrons and eventually leads to increase of the kinetic energy of electrons. Accordingly, with the reduction of the particle radius, the band gap also increased.[35]

Previous literature reports have described that the capability of light absorption of a photocatalyst is relative to the evaluation of the photocatalytic efficiency. However, it is worth noting that besides photoabsorption, other factors are also significant to enable an increasing photocatalytic efficiency of photocatalysts, such as the number of the effective active sites for photo-catalysis and the separation efficiency of photogenerated elec-tron–hole pairs.[36]

As shown in Fig. 8, the corresponding energy band gap of as-prepared $BiVO_4$ is around 2.45 eV, which proves to be in good agreement to the Kubelka–Munk band-gap estimation theory.[37] The relative position of the conduction band edge can be calculated according to the following eqn (1) and (2):

$$E_{CB} = \chi - E_f - 0.5E_g \qquad (1)$$
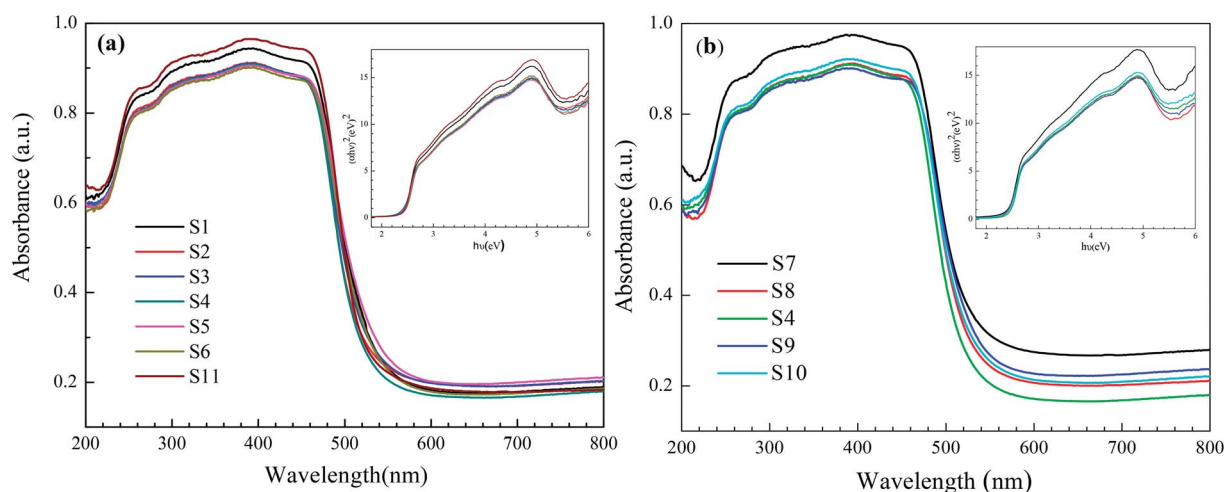
$$E_{VB} = E_{CB} + E_g \qquad (2)$$

Fig. 8 Typical diffuse-reflectance spectrum of the reticular $BiVO_4$ samples; the inset is the $(\alpha h\nu)^2$ to $h\nu$ curve: (a) different EDTA to CA, (b) different pH values.

Table 3 Photoluminescence properties and k_{app} of the reticular $BiVO_4$ samples

| Sample		E_g	E_{CB}	E_{VB}	k_{app}/min^{-1}	R^2
EDTA to CA	S1	2.42	0.33	2.75	0.0333	0.999
	S2	2.41	0.34	2.75	0.0606	0.999
	S3	2.42	0.33	2.75	0.08585	0.999
	S4	2.45	0.32	2.77	0.0947	0.999
	S5	2.43	0.33	2.76	0.1039	0.999
	S6	2.45	0.32	2.77	0.07808	0.999
	S11	2.46	0.31	2.77	0.01414	0.999
pH value	S7	2.41	0.34	2.75	0.06964	0.999
	S8	2.42	0.33	2.75	0.10266	0.999
	S4	2.45	0.32	2.77	0.0947	0.999
	S9	2.41	0.34	2.75	0.07808	0.999
	S10	2.42	0.33	2.75	0.06433	0.998

where χ represents the absolute electronegativity of the semiconductor, which is defined as the geometric mean of the absolute electronegativity of the constituent atoms. Herein, it can be calculated by the arithmetic mean of the atomic electron affinity and the first ionization energy. For $BiVO_4$, the value of χ was determined to be 6.04. E_f is the energy of free electrons on the hydrogen scale (about 4.5 eV); E_g is the band gap of the semiconductor which can be obtained from Fig. 8. Meanwhile, E_{CB} represents the conduction band potential and E_{VB} is the valence band potential. According to the above equations, the calculated top of the E_{VB} position and the calculated bottom of the E_{CB} position of $BiVO_4$ are showed in Table 3.

In a photocatalytic reaction, the activity is largely affected by the recombination of the photoinduced electrons and holes, ultimately decreasing the quantum yield. Due to the direct result of recombination of the free carriers, recording photoluminescence emission spectra can be regarded as an effective approach in an effort to understand the separation capacity of the photoinduced carriers.[38] The higher PL intensity usually suggests a lower separation efficiency of a photo-induced electron–hole and less photocatalytic performance. The PL spectra of $BiVO_4$ samples exhibit an excitation wavelength of 240 nm as

presented in Fig. 9. Furthermore, a sharp blue-green emission band centered at 484 nm can be observed, which are believed to be directly related to the charge transfer within the $[VO_4^{2-}]$ group. In addition, one broad green emission around 550 nm is observed. A similar phenomenon is also found in another report found in the literature.[39] Obviously, with different pH values and EDTA to CA ratios, the emission center is not altered. However, the PL intensities are enhanced first and then lowered as shown in Fig. 9. Presumably, the luminescent results coincide with the photocatalytic activities as described in the following section.

3.5. Photocatalytic performance

The photocatalytic activity of the prepared reticular $BiVO_4$ photocatalyst is evaluated by the degradation of a MB solution under visible light irradiation. The relationship between C/C_0 and the reaction time are shown in Fig. 10. It can be determined that the self-degradation of MB is negligible in the absence of a photocatalyst, indicating that any photolysis effects may be negligible. The adsorption of MB on the reticular $BiVO_4$ samples in the dark are also evaluated. After 50 min, the concentrations of MB remained unchanged, suggest that the decolorizations of MB by the reticular $BiVO_4$ samples are mainly caused by photodegradation but not adsorption. The reticular $BiVO_4$ samples show an increased visible light photocatalytic activity than the $BiVO_4$ samples prepared by the conventional sol–gel methods. About 98% degradation of MB can be observed after 50 min in the presence of the reticular $BiVO_4$ samples. The reason for this finding may be due to the fact that reticular $BiVO_4$ samples exhibit a smaller grain size and mesoporous structure, ultimately enhancing the absorption ability and increasing the separation efficiency of the photon-generated carriers. Furthermore, the reticular structures exhibit porosity, which reduces the diffusion length and improves the accessibility of active sites by the reactants. Additionally, the multiple reflections within the reticular cavity enhance efficient use of the light source, leading to the production of more photogenerated
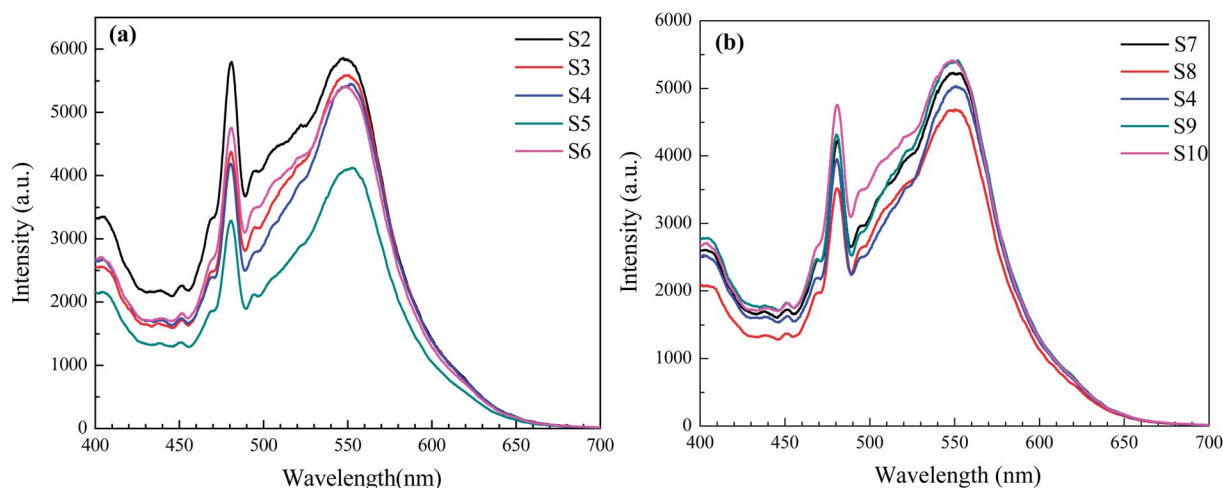
Fig. 9 PL spectra of the reticular $BiVO_4$ samples:(a) different EDTA to CA, (b) different pH values.
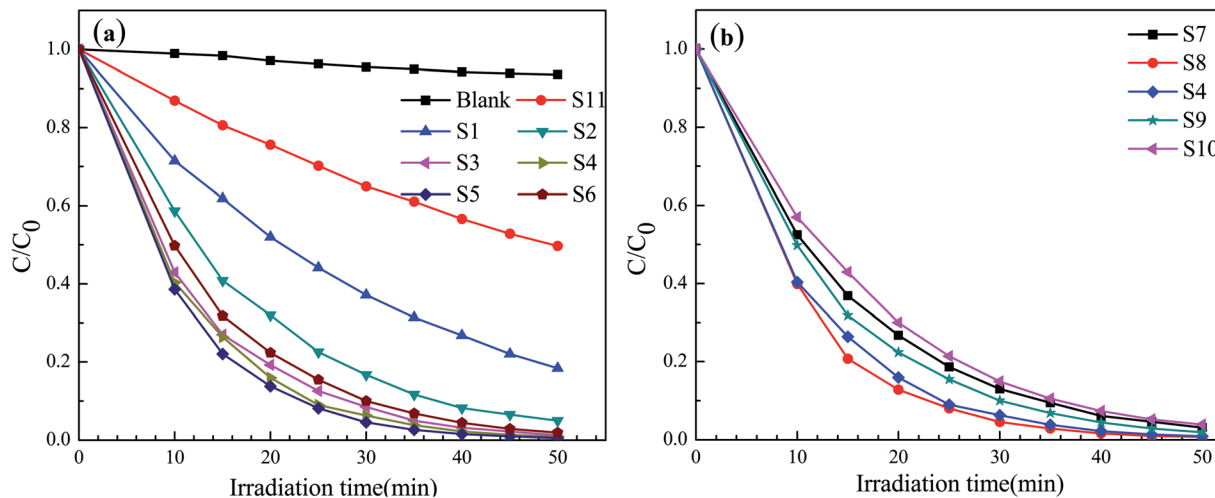
Fig. 10 Photocatalytic degradation efficiencies of MB:(a) different EDTA to CA, (b) different pH values.

charge carriers in comparison with the conventional morphology.[4,40,41]

Moreover, we have demonstrated that the photocatalytic degradation of MB by the BiVO$_4$ photocatalysts follows a pseudo-first-order reaction kinetics behavior when the pollutant was within a millimolar concentration range. The pseudo-first-order reaction kinetics can be expressed as follows: $\ln(C_0/C) = k_{app}t$, where k_{app} is the apparent reaction rate constant (min^{-1}), C_0 is the initial MB concentration (after sitting in the dark for 50 min), and C is the MB concentration at irradiation time t (min). The linear plots of $\ln(C_0/C)$ *versus* irradiation time t (min) for the degradation of MB are shown in Fig. 11. Here, it was determined that the relationships between $\ln(C_0/C)$ and irradiation time t are indeed linear. The apparent reaction constant k_{app} was used to evaluate the degradation rate as shown in Table 3. The rate constant of the S4 sample (0.0947 min^{-1}) was about 6 times as high as that of the S11 (0.01414 min^{-1}). Therefore, the obtained apparent reaction rate

constant k_{app} of the reticular BiVO$_4$ samples were much higher than that of S11 sample synthesized by the citric acid sol–gel method. Noteworthy, the enhanced photocatalytic activity of the reticular BiVO$_4$ samples can be attributed to the smaller grain size, mesoporous structure and relatively high specific surface area. The smaller grain size and mesoporous structure may reduce the migration length of the photon-generated carriers and further reduce the recombination rate of the photo-generated electron–hole pairs. The relatively high specific surface area provides more active sites, which are advantageous for the catalytic reaction. In addition, the photocatalytic property of monoclinic BiVO$_4$ is related to the distortion of the Bi–O polyhedron. The reticular samples are composed of hundreds of nanorods with relatively large distortion of the unit cell due to large surface strain effects.[42–44]

In view of these above results, a possible photocatalytic mechanism for the superior photocatalytic performance of the reticular BiVO$_4$ photocatalyst can be proposed by considering
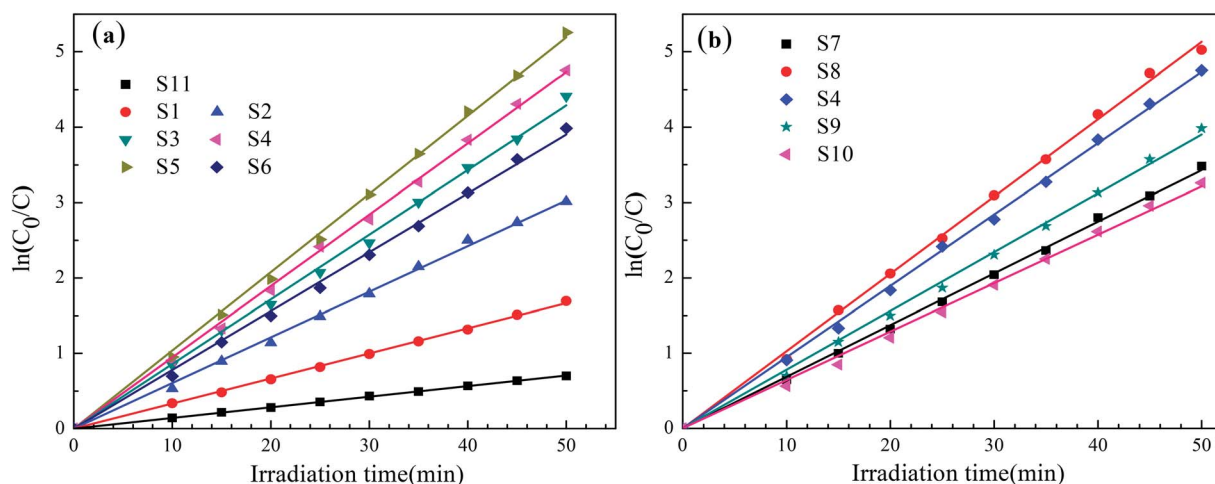

Fig. 11 The relationship between $\ln(C_0/C)$ and irradiation time t (min) of the reticular BiVO$_4$ samples: (a) different EDTA to CA, (b) different pH values.
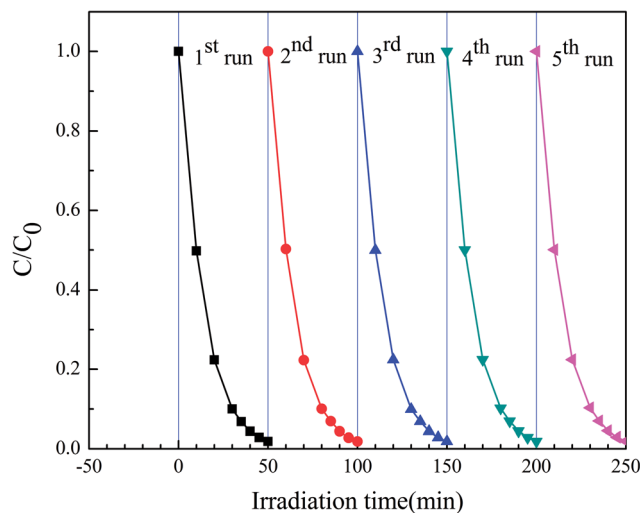
Fig. 12 Cycling runs for photocatalytic degradation of MB in the presence of S4 sample under visible-light.

the charge transfer process. Visible light excitation of the reticular BiVO$_4$ photocatalyst generates energized electrons (e$^-$) and positively charged holes (h$^+$). The photogenerated holes can react directly with H$_2$O and OH$^-$ to generate ·OH hydroxyl radicals, which play a central role in the degradation of the MB. Meanwhile, the photogenerated electrons will be caught by O$_2$ adsorbed on the surface of BiVO$_4$ acting as active sites to produce ·O^{2-} superoxide radicals. Besides, the reticular architecture assemble from hundreds of nanorods also indicated that the enlarged length provides highways for the charge transport along the originated nanorods, which leaded to an improved separation efficiency of photo-generated charge carriers. Thus, a higher photocatalytic activity was enhanced due to the effective inhibition of the recombination between electrons and holes.[19,45]

In order to evaluate the stability of this highly efficient photocatalyst species obtained, S4 sample were used in subsequent photocatalytic reactions. The photocatalysts were employed in five consecutive photocatalytic experiments, with the experimental procedure being similar to that described in the experimental section. However, in this particular case, after each photocatalytic reaction, the photocatalyst was filtered, dried and reused in a new reaction. As shown in Fig. 12, the photocatalytic efficiency of the reticular BiVO$_4$ samples did not exhibit a major reduction even after five recycles and only a slight decrease in photodegradation efficiency over time was observed. These results indicate that the reticular BiVO$_4$ samples were relatively stable and did not photocorrode during the photocatalytic process. The reticular BiVO$_4$ samples exhibit a high stability and excellent reusability in this catalytic process, a potentially critical feature for practical applications.

4.   Conclusions

In this study, reticular BiVO$_4$ catalysts composed of nanorods were successfully synthesized *via* a modified sol–gel

combustion method. Furthermore, the effects of pH values and EDTA to CA ratios on the structure and morphology of the samples were studied in detail. It was found that EDTA and pH play an important role in determining the morphology of the as-prepared BiVO$_4$ samples. Photocatalytic evaluation revealed that the reticular BiVO$_4$ samples exhibited high photocatalytic performance characteristics. For the degradation of methylene blue (MB) under visible-light irradiation, about 98% of the MB was found to be degraded within 50 min. Moreover, it was found that the degradation kinetics of MB was in good agreement with pseudo-first-order kinetics. The obtained apparent reaction rate constant k_{app} of the reticular BiVO$_4$ samples were much higher than that of the BiVO$_4$ samples synthesized by the citric acid sol–gel method. The simple synthetic method presented here uses only inexpensive reagents and might therefore be suitable for the large-scale commercially applications of reticular BiVO$_4$ samples as a highly active visible-light-driven photocatalysts.

Conflicts of interest

There are no conflicts to declare.

Acknowledgements

References

1 A. Kuback, M. Fernandez-García and G. Colon, *Chem. Rev.*, 2012, **112**, 1555–1614.
2 A. Asghar, A. A. A. Raman and W. M. A. W. Daud, *J. Cleaner Prod.*, 2015, **87**, 826–838.
3 W. Wang, M. O. Tade and Z. P. Shao, *Chem. Soc. Rev.*, 2015, **44**, 5371–5408.
4 C. C. Nguyen, N. N. Vu and T. O. Do, *J. Mater. Chem. A*, 2015, **3**, 18345–18359.
5 J. Liu and G. K. Zhang, *Phys. Chem. Chem. Phys.*, 2014, **16**, 8178–8192.
6 K. Wenderich and G. Mul, *Chem. Rev.*, 2016, **116**, 14587–14619.
7 X. B. Chen and S. S. Mao, *Chem. Rev.*, 2007, **107**, 2891–2959.
8 H. B. Yao, M. H. Fan, Y. J. Wang, G. S. Luo and W. Y. Fei, *J. Mater. Chem. A*, 2015, **3**, 17511–17524.
9 S. Takeshita, T. Isobe, T. Sawayama and S. Niikura, *Prog. Cryst. Growth Charact. Mater.*, 2011, **57**, 127–136.
10 Z. Q. Li, X. T. Chen and Z. L. Xue, *CrystEngComm*, 2013, **15**, 498–508.
11 J. J. Wang, L. Tang, G. M. Zeng, Y. C. Deng, Y. N. Liu, L. L. Wang, Y. Y. Zhou, Z. Guo, J. J. Wang and C. Zhang, *Appl. Catal., B*, 2017, **209**, 285–294.
12 A. Martinez-de la Cruz and U. M. Garcia Perez, *Mater. Res. Bull.*, 2010, **45**, 135–141.

13 L. W. Shan, G. L. Wang, J. Suriyaprakash, D. Li, L. Z. Liu and L. M. Dong, *J. Alloys Compd.*, 2015, **636**, 131–137.

14 T. Saison, N. Chemin, C. Chaneac, O. Durupthy, V. Ruaux, L. Mariey, F. Mauge, P. Beaunier and J. P. Jolivet, *J. Phys. Chem. C*, 2011, **115**, 5657–5666.

15 J. Q. Yu, Y. Zhang and A. Kudo, *J. Solid State Chem.*, 2009, **182**, 223–228.

16 R. A. He, S. W. Cao, P. Zhou and J. G. Yu, *Chin. J. Catal.*, 2014, **35**, 989–1007.

17 C. N. Van, W. S. Chang, J. W. Chen, K. A. Tsai, W. Y. Tzeng, Y. C. Lin, H. H. Kuo, H. J. Liu, K. D. Chang, W. C. Chou, C. L. Wu, Y. C. Chen, C. W. Luo, Y. J. Hsu and Y. H. Chu, *Nano Energy*, 2015, **15**, 625–633.

18 J. Yu and A. Kudo, *Adv. Funct. Mater.*, 2006, **16**, 2163–2169.

19 M. Wang, P. Y. Guo, T. Y. Chai, Y. H. Xie, J. Han, M. Y. You, Y. Z. Wang and T. Zhu, *J. Alloys Compd.*, 2017, **691**, 8–14.

20 R. G. Chaudhuri and S. Paria, *Chem. Rev.*, 2012, **112**, 2373–2433.

21 M. Wang, Q. Liu, Y. S. Che, L. F. Zhang and D. Zhang, *J. Alloys Compd.*, 2013, **548**, 70–76.

22 W. Liu, X. F. Wang, L. X. Cao, G. Su, L. Zhang and Y. G. Wang, *Sci. China: Chem.*, 2011, **54**, 724–729.

23 C. Y. Chung and C. H. Lu, *J. Alloy. Compd*, 2010, **502**, L1–L5.

24 T. D. Nguyen, C. T. Dinh and T. O. Do, *Langmuir*, 2009, **25**, 11142–11148.

25 U. M. García-Pérez, S. Sepúlveda-Guzmán and A. Martínez-de la Cruz, *Solid State Sci.*, 2012, **14**, 293–298.

26 N. Wang, Q. F. Zhang and W. Chen, *Cryst. Res. Technol.*, 2007, **42**, 138–142.

27 J. F. Liu and Y. D. Li, *J. Mater. Chem.*, 2007, **17**, 1797–1803.

28 L. Zhou, W. Z. Wang, L. S. Zhang, H. L. Xu and W. Zhu, *J. Phys. Chem. C*, 2007, **111**, 13659–13664.

29 S. M. Sun, W. Z. Wang, L. Zhou and H. L. Xu, *Ind. Eng. Chem. Res.*, 2009, **48**, 1735–1739.

30 Z. F. Zhu, J. Du, J. Q. Li, Y. L. Zhang and D. G. Liu, *Ceram. Int.*, 2012, **38**, 4827–4834.

31 F. Luo, C. J. Jia, W. Song, L. P. You and C. H. Yan, *Cryst. Growth Des.*, 2005, **5**, 137–142.

32 P. Madhusudan, J. Ran, J. Zhang, J. G. Yu and G. Liu, *Appl. Catal., B*, 2011, **110**, 286–295.

33 W. Z. Yin, W. Z. Wang, L. Zhou, S. M. Sun and L. Zhang, *J. Hazard. Mater.*, 2010, **173**, 194–199.

34 L. Chen, J. X. Wang, D. W. Meng, Y. L. Xing, X. Y. Tian, X. H. Yu, K. Xu and X. L. Wu, *J. Sol-Gel Sci. Technol.*, 2015, **76**, 562–571.

35 M. Wang, C. Niu, J. Liu, Q. W. Wang, C. X. Yang and H. Y. Zheng, *J. Alloys Compd.*, 2015, **648**, 1109–1115.

36 Y. F. Zhang, M. Park, H. Y. Kim and S. J. Park, *J. Alloys Compd.*, 2016, **686**, 106–114.

37 H. Y. Li, Y. J. Sun, B. Cai, S. Gan, D. Han, L. Niu and T. Wu, *Appl. Catal., B*, 2015, **170–171**, 206–214.

38 S. Y. Wu, H. Zheng, Y. W. Lian and Y. Wu, *Mater. Res. Bull.*, 2013, **48**, 2901–2907.

39 H. F. Cheng, B. B. Huang, Y. Dai, X. Y. Qin and X. Y. Zhang, *Langmuir*, 2010, **26**, 6618–6624.

40 Y. X. Liu, H. X. Dai, J. G. Deng, L. Zhang and C. T. Au, *Nanoscale*, 2012, **4**, 2317–2325.

41 N. Muthuchamy, K. P. Lee and A. I. Gopalan, *Biosens. Bioelectron.*, 2017, **89**, 390–399.

42 J. T. Li and N. Q. Wu, *Catal. Sci. Technol.*, 2015, **5**, 1360–1384.

43 T. Yang, D. G. Xia, G. Chen and Y. Chen, *Mater. Chem. Phys.*, 2009, **114**, 69–72.

44 G. S. Liu, S. W. Liu, Q. F. Lu, H. Sun, F. Xu and G. Zhao, *J. Sol-Gel Sci. Technol.*, 2014, **70**, 24–32.

45 S. M. Thalluri, M. Hussain, G. Saracco, J. Barber and N. Russo, *Ind. Eng. Chem. Res.*, 2014, **53**, 2640–2646.